Progress In Electromagnetics Research B, Vol. 44, 137–161, 2012

A NOVEL NONUNIFORM SUBGRIDDING SCHEME FOR FDTD USING AN OPTIMAL INTERPOLATION TECHNIQUE

G. Kim[1], E. Arvas[1], V. Demir[2, *], and A. Z. Elsherbeni[3]

[1]Department of Electrical Engineering and Computer Science, Syracuse University, Syracuse, NY 13244, USA

[2]Department of Electrical Engineering, Northern Illinois University, DeKalb, IL 60115, USA

[3]Department of Electrical Engineering, University of Mississippi, University, MS 38677, USA

Abstract—Finite-Difference Time-Domain (FDTD) subgridding schemes can significantly improve efficiency of various electromagnetic circuit simulations. However, numerous subgridding schemes suffer from issues associated with stability, efficiency, and material traverse capability. These issues limit general applicability of FDTD subgridding schemes to realistic problems. Herein, a robust nonuniform subgridding scheme is presented that overcomes those weaknesses. The scheme improves simulation accuracy with the aid of greatly increased stability margin and an optimal interpolation technique. It also improves simulation efficiency by allowing the use of time step factors as close as the Courant-Friedrichs-Lewy (CFL) limit. In addition, late-time stability and general applicability are verified through practical microstrip circuit simulation examples.

1. INTRODUCTION

The finite-difference time-domain (FDTD) method is a very attractive numerical tool to solve various electromagnetic problems for its simplicity of straightforward implementation and capability of handling complex geometries [1]. Recent rapid development of computer technology has led to extensive applications using the FDTD method. Researches have shown that subgridding approach can

Received 10 July 2012, Accepted 17 September 2012, Scheduled 20 September 2012

* Corresponding author: Veysel Demir (vdemir@niu.edu).

improve efficiency and accuracy of the standard FDTD algorithm dramatically. Subgridding scheme has been under great attention during the past two decades, as a consequence, numerous promising subgridding schemes have been developed and a number of remarkable results have come out.

Overall performance and robustness of a certain subgridding scheme can be evaluated based on following key aspects:

(i) *Accuracy*, which mainly depends on a coupling method and reflection level at the interface between main-grid (MG) and sub-grid (SG) regions.

(ii) *Efficiency*, which is directly associated with the complexity of coupling scheme and the use of Courant-Friedrichs-Lewy (CFL) time step limit [2].

(iii) *Stability* that determines practical usefulness.

(iv) *General applicability* represented by material traverse capability, especially for thin PEC plates.

(v) *Simplicity* that ensures easy integration of subgridding scheme into the standard FDTD algorithm.

Some aspects are interconnected with a trade-off relation, so other performance factors are frequently sacrificed if one aspect is intensively pursued. For instance, emphasis on ensuring no late-time instability often deteriorates simulation accuracy and efficiency. Nevertheless, a general goal in the development of a subgridding algorithm is to achieve high level of performance and robustness in all of the key aspects mentioned above. Many of the published subgridding methods show their own advantageous features. Simultaneously, each subgridding scheme also has its own limitations or weaknesses that were relatively disregarded for reinforcing certain beneficial aspects. A few subgridding schemes were developed focusing on stability. Thoma and Weiland presented a consistent 3-D subgridding scheme using the finite integration technique in [3]. Krishnaiah and Railton also proposed a similar consistent coupling method by introducing an equivalent passive circuit model in [4]. Both methods used linearly interpolated tangential magnetic field components as boundary conditions of the SG region. For temporal interpolation, the former used nearest neighbor method, and linear interpolation in time was implemented in the latter. The former and the latter adopted different refinement factors of $1 : 2$ and $1 : 3$, respectively. A reduced CFL number by a factor of two was chosen for a stable result in [3], but it was not reported in [4].

Xiao et al. proposed an explicit 3-D subgridding algorithm based on the interpolation of current density distribution in [5]. A stable

subgridding scheme could be achieved by maintaining the consistency and symmetry of forward (from MG to SG) and backward (from SG to MG) couplings. Later, their method was improved in [6] by introducing the separation of temporal and spatial interfaces. The nearest neighbor interpolation in time given in [3] was adopted in [6], and the CFL factor used in their numerical experiments was not reported.

Subgridding schemes [3–6] successfully achieved the goal of stability, however, they have poor general applicability associated with material discontinuities at the interfaces or require additional special treatment to obtain it. Chilton and Lee, utilizing the "simple" interpolation method [7], developed a conservative and probably stable subgridding scheme based on the finite element principles in [8]. This subgridding algorithm can accomplish not only the probable stability but also the material traverse capability due to the property of the interpolation method. Using analytical discrete operator approach and constructed coupling stencil matrix, the conservative spatial interpolation method was presented. However, an identical time increment for both MG and SG was used in the leapfrog time integration, i.e., no temporal interpolation was dealt with in [8]; this deteriorates the overall simulation efficiency significantly. Moreover, its implicit update process makes the implementation of the proposed spatial interpolation very complex.

There has been strong interest in the development of a subgridding scheme to allow traversing inhomogeneous regions including dielectric and PEC discontinuities at the MG-SG interface. This is an important issue related to the accuracy and stability as well as general applicability. In 1997, Chevalier et al. proposed the subgridding method with PEC traverse capability in [9]. Magnetic field components were interpolated for an odd number of refinement factors, and a modified linear interpolation method was provided for special treatment of PEC traversing MG-SG interfaces. The used CFL factor was reduced to 0.71 for maintaining stability. In 2001, White et al. published the subgridding method [10] having dielectric traverse capability by the use of a weighted function, which is dependent on material properties. They provided a general method applied to any number of refinement factors. However, this subgridding method can be regarded as the one to use piecewise-constant interpolation in both tangential and normal directions only if material parameters are well-approximated by proper sub-cell averaging as in Chapter 3 of [1]. In addition, the method reveals weakness in the presence of a thin PEC plate traversing the boundary interface.

In this paper, we pursue a new subgridding scheme showing satisfactory performance in all of the aforementioned key aspects. To

this end, a novel nonuniform sub-grid mesh configuration is proposed and its apparent benefit to increase the stability margin is verified. By the combination of the mesh configuration and coupling of magnetic field components, a robust subgridding scheme is developed and superior performances are validated through realistic microstrip circuit simulation examples.

2. A NOVEL NONUNIFORM SUB-GRID MESH

Comparing a subgridding scheme with a uniform FDTD algorithm, we can see that the subgridding scheme has additional numerical errors. These errors have been discussed in [11–14]. Especially [12] explains three numerical error sources degrading subgridding accuracy: (i) spatial frequency aliasing, (ii) high frequency cutoff, and (iii) numerical impedance mismatch. To enhance subgridding accuracy, digital filtering and phase compensation techniques were presented in [12].

In the perspective of subgridding functional operation, the aliasing (i) can be explained in terms of coupling (interpolation/decimation [12]) and dislocation [13] errors. The coupling and dislocation errors belonging to the aliasing and the numerical impedance mismatch at the MG-SG interface are crucial sources affecting subgridding accuracy. An accurate subgridding scheme requires minimizing numerical errors, but late-time instability is often unavoidable in most of high-accuracy schemes, e.g., [13, 14] mitigating aliasing and impedance mismatch, respectively. On the other hand, it has been reported that late-time stable schemes show relatively poor reflection performance due to the strict constraint of keeping coupling symmetry as in [3]. Therefore, the most desirable subgridding scheme should hold a high level of accuracy as well as stability, and the two contradictory aspects might be accomplished by securing long-term stability even without the aid of the strict symmetry constraint.

To this end, simply consider interpolation and dislocation errors. For a stable solution, it is necessary that any numerical errors must not be accumulated as a wave propagates in both time and space. An interpolation error occurs when missing SG field values are approximated from MG samples, and a dislocation error appears in the updating process of field components when other fields needed for the updating are not collocated. Generally both errors are mingled at the same MG-SG boundary interface plane and undermine subgridding stability as well as accuracy. If these two error-source planes are separated properly, it may be advantageous to achieve a more stable subgridding scheme minimizing accuracy degradation. This is the basic

motivation for this paper which presents a new nonuniform sub-grid mesh configuration.

Hereinafter, a refinement factor of 3 is assumed for simplicity though other mesh ratios can be applied easily. Also it is noted that uppercase "E" and "H" and subscript "m" indicate MG variables, whereas lowercase "e" and "h" and subscript "s" denote SG variables. Basically, a nonuniform sub-grid mesh is generated by embedding a nonuniform mesh with denser resolution within a uniform coarse mesh region. Consider a simple 2-D problem space which is composed of $6\Delta x_m \times 6\Delta y_m$ MG uniform cells, and suppose that finer mesh is necessary in the central region of $2\Delta x_m \times 2\Delta y_m$. A typical nonuniform mesh and a uniform sub-grid are shown in Figs. 1(a) and 1(b), respectively. In Fig. 1, gray lines represent main meshes and dashed lines represent sub meshes, while overlapping meshes between main and sub meshes are illustrated by black solid lines.

As shown in Fig. 1(a), a nonuniform mesh doesn't have any sub region, but the problem space is composed of only one main grid which is meshed nonuniformly. On the other hand, Fig. 1(b) has a uniform-

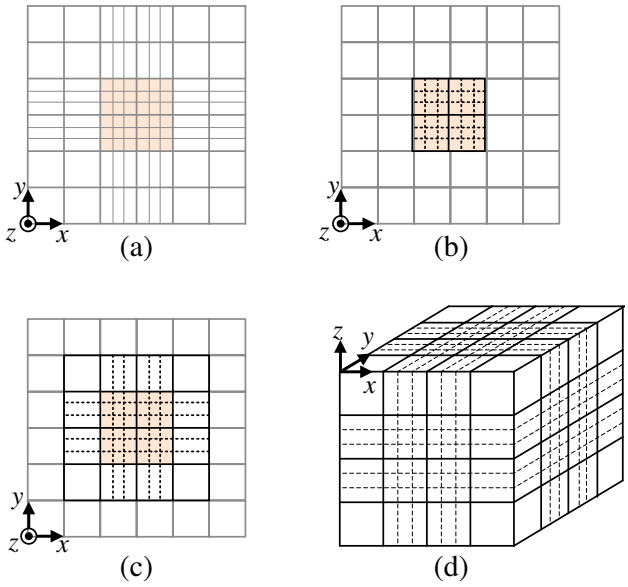

Figure 1. Comparison of three different mesh configurations, (a) nonuniform mesh, (b) uniform sub-grid mesh, (c) nonuniform sub-grid mesh, and (d) 3-D illustration of the nonuniform sub-grid mesh region.

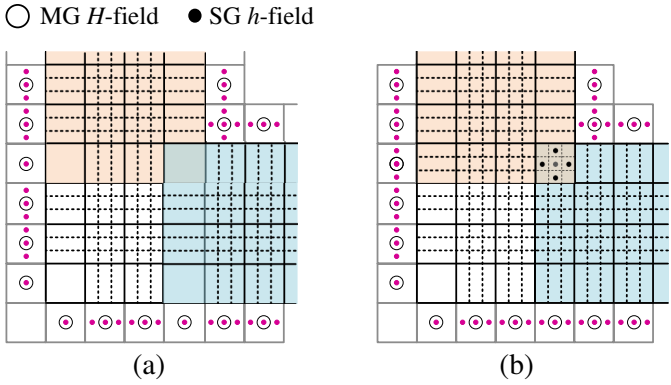

Figure 2. Extension of the nonuniform sub-grid mesh to a sub-grid region with a re-entrant corner, (a) a straightforward composition, and (b) an alternative composition.

grid main mesh, and a local part of entire domain is defined as another uniform-grid region having finer resolution. Based on the mesh schemes in Figs. 1(a) and 1(b), it is possible to construct a different sort of sub-grid mesh, which is shown in Fig. 1(c). We call this a nonuniform sub-grid (NSG), and its three-dimensional illustration is shown in Fig. 1(d). The NSG mesh configuration can be expanded to more complex cases such as a sub-grid region with re-entrant corners. For instance, an L-shaped region can be replaced by three separated NSG meshes. Fig. 2(a) depicts the straightforward combination of three rectangular sub-grids. If the uniform mesh transition around an overlapping region is preferred for lower numerical dispersion, the combination shown in Fig. 2(b) can be considered. But special treatment is required to obtain four SG h-field components located within an overlapping cell.

Unlike a conventional uniform sub-grid (USG) mesh, the NSG mesh can separate the interpolation-error and dislocation-error planes. This advantageous feature is illustrated in Fig. 3, where solid and dashed lines outside the meshes denote where dislocation and interpolation errors occur, respectively. In the NSG mesh configuration, interpolation and dislocation errors are separated as shown in Figs. 3(c) and 3(d), while they coincide at the same plane and are added up together at the interface in the USG mesh as shown in Figs. 3(a) and 3(b). Furthermore, two error-source planes are completely separated in the NSG with H-coupling (NSG-H), whereas two errors are mingled in the updating of SG h-fields between two error planes in the NSG with E-coupling (NSG-E). Therefore, the new NSG-H scheme provides a greatly increased stability margin and it will

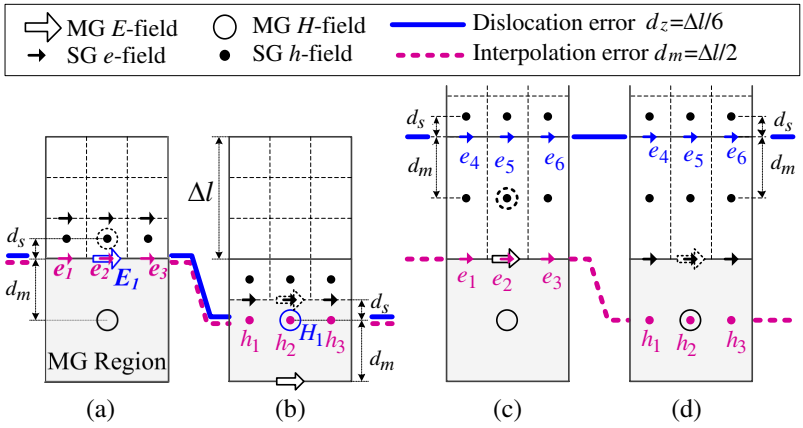

Figure 3. Separation of interpolation and dislocation errors in a nonuniform sub-grid mesh configuration, (a) uniform sub-grid with E-coupling (USG-E), (b) uniform sub-grid with H-coupling (USG-H), (c) nonuniform sub-grid with E-coupling (NSG-E), and (d) nonuniform sub-grid with H-coupling (NSG-H).

be verified in numerical experiments that a late-time stable solution can be achieved without implementing the strict coupling symmetry condition.

3. NONUNIFORM SUBGRIDDING ALGORITHM

Advantageous features of the uniform subgridding schemes [3–10] are inherited for the development of a new robust subgridding scheme. The nearest neighbor interpolation is used as *the consistent coupling method* in time [3]. To be able to get rid of instability factor in time and to facilitate the implementation of a stable subgridding scheme, *the separation of temporal and spatial interface* [6] is also adopted in the NSG scheme. Based on temporal and spatial coupling schemes, similar recursive updating algorithms to [3, 4, 6] can be used. Special treatments due to the new NSG mesh configuration are required only in the spatial coupling algorithm, and they are explained with respect to MG E-field and H-field couplings in the following sections.

3.1. Nonuniform Subgridding Scheme with *E*-coupling

In the NSG-E scheme, interpolation for obtaining missing SG e-fields, which is often called forward coupling, is performed piecewise-

constantly [7] in a *tangential* direction (T^C). A piecewise-*linear* method is used in a *normal* direction (N^L) to E-field directions. The constant and linear interpolation is referred to as a $T^C N^L$ method here. It is noted that the $T^C N^L$ method can overcome material discontinuities across the interface boundary because interpolation execution is confined within one MG cell.

Consider $T^C N^L$ interpolation near the facet position of the MG-SG interface box. Fig. 4 shows electric field components and their couplings on the x-z interface plane, i.e., the front face of the 3-D

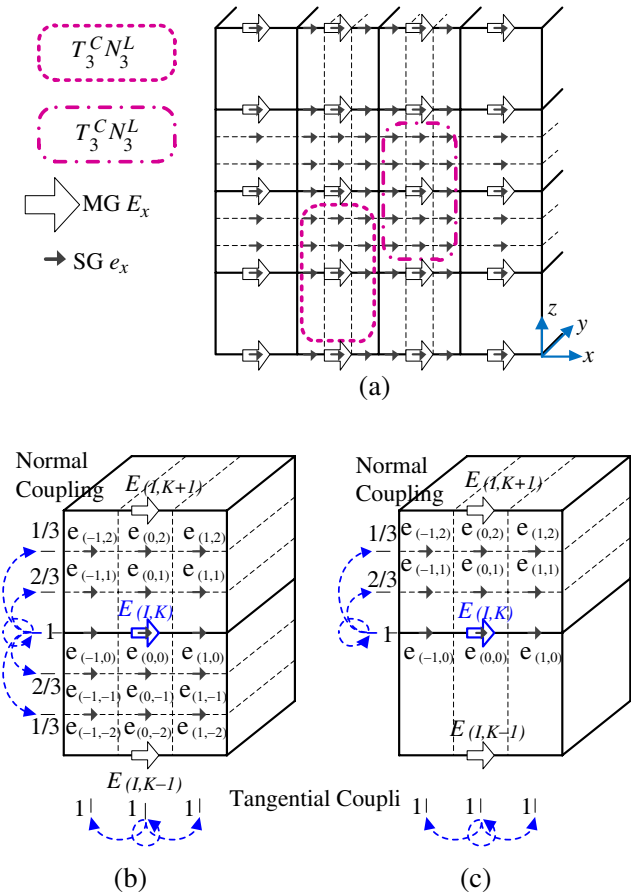

Figure 4. (a) Electric field components on x-z interface plane, (b) $T_3^C N_5^L$, and (c) $T_3^C N_3^L$ forward couplings at the interface along tangential and normal directions.

interface box. $T^C N^L$ forward coupling at the interface facet position can be divided into $T_3^C N_5^L$ and $T_3^C N_3^L$ by the number of SG e-field components interpolated from one MG E-field sample. In the uniform SG area, one E-field sample has influence tangentially on 3 SG components and normally on 5 SG components. In the non-uniform SG area, a MG E-field sample is utilized for the interpolation of only 3 SG components along the normal direction. Two forward coupling schemes are illustrated with normal and tangential coupling coefficients in Figs. 4(b) and 4(c). If this fact is considered properly, the other process of the consistent coupling will be preceded with ease.

As pointed out in [3–6], *backward coupling*, which determines missing MG H-fields from calculated SG h-field components, is required to be *symmetric* to the $T^C N^L$ forward coupling in order to avoid late-time instability. Fig. 5 depicts the symmetric backward coupling. Note that the consistent coupling can be accomplished easily because any dislocation error does not appear in the coupling process. In Fig. 5, the updating equation for $E_x^{n+1}(I,J,K)$ is given as,

$$\begin{aligned} E_x^{n+1}(I,J,K) &= C_{exe}(I,J,K) \times E_x^n(I,J,K) \\ &+ C_{exhy}(I,J,K) \times \left[H_y^{n+\frac{1}{2}}(I,J,K) - H_y^{n+\frac{1}{2}}(I,J,K-1) \right] \\ &+ C_{exhz}(I,J,K) \times \left[\tilde{H}_z^{n+\frac{1}{2}}(I,J,K) - H_z^{n+\frac{1}{2}}(I,J-1,K) \right], \end{aligned} \quad (1)$$

where updating coefficients are denoted by $C(I,J,K)$, and the details can be seen in [1]. An unknown MG H-field component is denoted

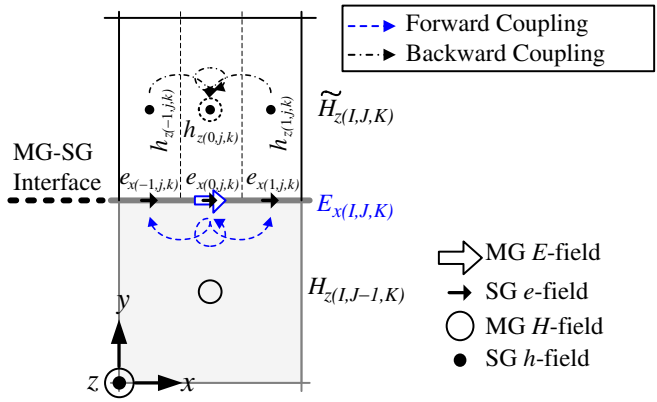

Figure 5. $T^C N^L$ forward and backward couplings in a nonuniform subgridding scheme.

by $\tilde{H}_z^{n+\frac{1}{2}}(I,J,K)$, which is determined by the backward coupling that takes the average of relevant SG h-field components in a consistent way. The symmetric backward coupling can be expressed using general matrix-form arrays, such as a forward coupling coefficient matrix T along a tangential direction, a forward coupling coefficient matrix N along a normal direction, an associated SG h-field matrix $[[h_z^{n+\frac{1}{2}}]]$, and normalizing factor G as,

$$\tilde{H}_z^{n+\frac{1}{2}}(I,J,K) = G_{CL,F}^{K,z} \times \mathbb{T}^T \cdot \left[\left[h_z^{n+\frac{1}{2}}\right]\right] \cdot \mathbb{N}^T. \tag{2}$$

The forward coupling coefficient matrix $\mathbb{T}$ and $\mathbb{N}$ are transposed in the backward coupling. This is a key factor to achieve a symmetric backward coupling as explained in [6]. Equation (2) can be rewritten as (3)–(4) and (5)–(6) in accordance with $T_3^C N_5^L$ and $T_3^C N_3^L$ forward couplings, respectively.

$$\begin{aligned}\tilde{H}_z^{n+\frac{1}{2}}(I,J,K) &= G_{CL,F35}^{K,z} \times \begin{bmatrix} 1 \\ 1 \\ 1 \end{bmatrix}^T \\ &\times \begin{bmatrix} h_{(-1,j,-2)} & h_{(-1,j,-1)} & h_{(-1,j,0)} & h_{(-1,j,1)} & h_{(-1,j,2)} \\ h_{(0,j,-2)} & h_{(0,j,-1)} & h_{(0,j,0)} & h_{(0,j,1)} & h_{(0,j,2)} \\ h_{(1,j,-2)} & h_{(1,j,-1)} & h_{(1,j,0)} & h_{(1,j,1)} & h_{(1,j,2)} \end{bmatrix}_Z^{n+\frac{1}{2}} \\ &\times \begin{bmatrix} \frac{1}{3} & \frac{2}{3} & 1 & \frac{2}{3} & \frac{1}{3} \end{bmatrix}^T, \end{aligned} \tag{3}$$

where

$$G_{CL,F35}^{K,z} = \frac{1}{\Sigma_{p=1}^3 \Sigma_{q=1}^5 [\mathbb{T}_3 \times \mathbb{N}_5]_{p,q}} = 1/9. \tag{4}$$

$$\begin{aligned}\tilde{H}_z^{n+\frac{1}{2}}(I,J,K) &= G_{CL,F35}^{K,z} \\ &\times \begin{bmatrix} 1 \\ 1 \\ 1 \end{bmatrix}^T \times \begin{bmatrix} h_{(-1,j,0)} & h_{(-1,j,1)} & h_{(-1,j,2)} \\ h_{(0,j,0)} & h_{(0,j,1)} & h_{(0,j,2)} \\ h_{(1,j,0)} & h_{(1,j,1)} & h_{(1,j,2)} \end{bmatrix}_Z^{n+\frac{1}{2}} \times \begin{bmatrix} 1 & \frac{2}{3} & \frac{1}{3} \end{bmatrix}^T, \end{aligned} \tag{5}$$

where

$$G_{CL,F35}^{K,z} = \frac{1}{\Sigma_{p=1}^3 \Sigma_{q=1}^3 [\mathbb{T}_3 \times \mathbb{N}_3]_{p,q}} = 1/6. \tag{6}$$

Herein the symmetric coupling scheme is discussed only at the facet position of 3-D interface box for simplicity. At other positions such as on an edge, the symmetry can be maintained in a similar way.

3.2. Nonuniform Subgridding Scheme with H-coupling

In this section, the NSG mesh configuration is combined with MG H-field interpolation. As shown in Fig. 3(d), the NSG-H scheme can have a more increased stability margin due to the complete separation of the two error planes. In addition, interpolation of MG H-field components allows higher robustness against material discontinuities in case that non-magnetic dielectric material is used at the interface boundary as described in [9].

Basically, SG h-field components are interpolated linearly along a normal direction to the cell facet plane where MG H-field is located. Interpolation along a normal direction is identical to the method adopted in the previous NSG-E scheme. For instance, h_z components are approximated linearly in z direction, for z direction is normal to the x-y cell facet plane.

Along the tangential direction, piecewise-constant interpolation was used in the NSG-E. This was an inevitable choice because other more accurate interpolations require more complex backward coupling. On the other hand, the NSG-H scheme is capable of dealing with other interpolation methods easily due to its robustness. A number of numerical experiments reveal that a stable subgridding scheme can be implemented using more accurate interpolation methods. In addition, the NSG-H scheme shows no late-time instability for sufficiently long time period even without the use of complex symmetric backward coupling scheme.

Among various interpolation techniques, piecewise-constant [7] and piecewise-quadratic [15] methods are selected by considering accuracy and efficiency. Other methods such as piecewise-linear and cubic/shape-preserving spline [15, 16] were also implemented, but practical simulations yielded some problems due to material discontinuities by the linear method and efficiency degradation by the spline methods. We consider two interpolation methods which are applied to the interpolation of MG H-field along a tangential direction to the cell facet. The goal is set to approximate the values of the z-directed h-fields h_{21}, h_{22}, and h_{23} in Fig. 6 using two interpolation techniques. The approximation of SG h-field components is simply given by piecewise-constant method (T^C) as

$$h_{21} = h_{22} = h_{23} = H_2. \tag{7}$$

On the other hand, piecewise-quadratic interpolation (T^Q) using a second order polynomial [15] is given in a general form as

$$h(\bar{x}) = (2\bar{x} - 1)(\bar{x} - 1)H_1 - 4\bar{x}(\bar{x} - 1)H_2 + \bar{x}(2\bar{x} - 1)H_3, \tag{8}$$

where $\bar{x}$ is the normalized position in the range $0 \leq \bar{x} \leq 1$, and $H_1 = H|_{\bar{x}=0}$, $H_2 = H|_{\bar{x}=0.5}$, $H_3 = H|_{\bar{x}=1}$. If (8) is applied to the

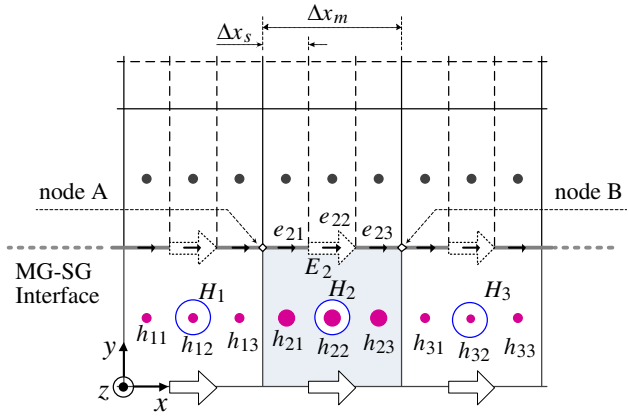

Figure 6. Approximation of h_z components by interpolation of H_z components along x direction.

case of refinement factor 3 in Fig. 6, then we have

$$h_{21} = \frac{1}{9}(8H_2 + 2H_1 - H_3), \quad h_{22} = H_2, \quad h_{23} = \frac{1}{9}(8H_2 + 2H_3 - H_1). \quad (9)$$

Using higher-order interpolation in (9), we can obtain more accurate results with little increase of computational cost than the piecewise-constant or -linear method.

The piecewise-constant and piecewise-quadratic interpolation methods in tangential directions are basically used for the forward coupling scheme. The implementation of symmetric backward coupling corresponding to each forward coupling is not trivial especially for the $T^Q N^L$ method. Fortunately, the NSG-H has a sufficient stability margin, thus the symmetric backward coupling scheme is substituted by a simple tangential averaging scheme that ensures equivalence between MG and SG. For voltage ΔV between nodes A and B in Fig. 6, the equivalence between MG and SG can be written as

$$\int_{L_2} \vec{E}_2 \cdot d\vec{l} = \int_{l_{21}} \vec{e}_{21} \cdot d\vec{l} + \int_{l_{22}} \vec{e}_{22} \cdot d\vec{l} + \int_{l_{23}} \vec{e}_{23} \cdot d\vec{l}. \quad (10)$$

The discretized form of (10) yields a simple backward coupling equation as

$$E_2 \cdot \Delta x_m = (e_{21} + e_{22} + e_{23}) \cdot \Delta x_s, \quad E_2 = (e_{21} + e_{22} + e_{23}). \quad (11)$$

Based on the simple backward coupling in (11), the NSG-H scheme employing different tangential interpolation methods are tested in a couple of examples. Late-time instability is not observed in both

$T^C N^L$ and $T^Q N^L$ interpolation methods, and details for stability tests will be discussed in the Section 4. This is obvious evidence that the stability margin is increased significantly in the NSG-H scheme. Furthermore, the scheme can provide accuracy improvement because it is not following by the symmetry restriction between forward and backward couplings. Definitely, complex symmetric backward coupling degrades simulation accuracy and requires more computation time. Accuracy estimations will be discussed in the following numerical experiments.

3.3. Accuracy Improvement Using an Optimal Interpolation Technique

If a sub-domain region is constructed within a problem space, there exist mainly two kinds of reflections along the main path of wave propagation, which are reflections from MG to SG and from SG to MG. Most of the existing subgridding methods give no attention to the reflection performance difference with respect to two types of wave propagation at the interface. Only the MG-to-SG reflection performance is taken into account. In our experience, $T^Q N^L$ and $T^C N^L$ result in better performance for the MG-to-SG and the SG-to-MG propagation modes, respectively. For the MG-to-SG mode, field information in the MG region is transferred into the SG region by a certain type of forward coupling at the interface, and reflection performance directly depends on the accuracy of the interpolation method. Thus, it is obvious that higher order interpolation methods perform better than simple ones. On the other hand, field information is transferred from the SG to the MG region by backward coupling for the SG-to-MG mode. In the implemented NSG-H scheme, there is no difference in the backward coupling with respect to each interpolation method. Reflection performance is determined by the degree of mismatch between the forward and the backward couplings. For instance, the constant scheme in (7) is well matched to the backward coupling in (11), while the quadratic scheme in (9) is less matched to the same backward coupling. Therefore, the optimal combination of different interpolation methods such as $T^Q N^L$ and $T^C N^L$ can yield more accurate results in the NSG-H scheme as long as each employed interpolation method can guarantee sufficiently long-term stability. Evaluation of reflection performance for both MG-to-SG and SG-to-MG paths is shown in following section.

For an interface with an apparent propagation mode, an optimal interpolation method can be fixed to $T^C N^L$ or $T^Q N^L$ based on predefined geometrical information such as sub-grid, source, and load locations. The $T^C N^L$ method is assigned to an interface mainly

functioning as a radiation boundary (from SG to MG), whereas the $T^Q N^L$ method is applied to an interface mainly functioning as an absorbing boundary (from MG to SG). For an interface with a mixed or ambiguous mode, an adaptive selection of optimal methods can provide better accuracy. Wave propagation status is monitored in a real-time manner, and optimal method is selected adaptively. To this end, energy level of unit cells in MG and SG near the interface is calculated using approximation [13] as

$$W^n_{(I,J,K)} \approx \frac{1}{2}\left[\varepsilon_{(I,J,K)}|\bar{E}^n_{(I,J,K)}|^2 + \mu_{(I,J,K)}|\bar{H}^n_{(I,J,K)}|^2\right] V_{(I,J,K)}, \quad (12)$$

where $V_{(I,J,K)}$ is MG unit cell volume, and $W^n_{(I,J,K)}$ is the energy confined in cell (I, J, K) at time step n. Thus, $\bar{E}^n_{(I,J,K)}$ and $\bar{H}^n_{(I,J,K)}$ are defined at the center of the cell, and averaged in time and space. Temporal and spatial gradients of the averaged energy are defined as

$$\nabla^S = \tilde{W}^n_{mg} - \tilde{W}^n_{sg}, \quad \nabla^T_{mg} = \tilde{W}^n_{mg} - \tilde{W}^{n-1}_{mg}, \nabla^T_{sg} = \tilde{W}^n_{sg} - W^{n-1}_{sg}, \quad (13)$$

where $\tilde{W}^n_{mg}$ and $\tilde{W}^n_{sg}$ represent the averaged energy of cells in MG and SG regions, respectively. ∇^S and ∇^T are spatial and temporal energy gradients. Using the calculated ∇^S and ∇^T, the boundary status is determined by following criteria: MG-to-SG if ∇^S has the opposite sign to both ∇^T_{mg} and ∇^T_{sg}, and SG-to-MG if all of them have the same sign. If the condition is not satisfied, current propagation condition is followed by the previously determined condition.

Using these strategies in the NSG-H scheme, overall simulation accuracy can be improved further with a little increase of computational cost. It is also noted that we do not consider several well-known methods, discussed in [17] and its references, to compensate degraded accuracy due to the nonuniform grid in the SG region, since most of these methods can worsen late-time instability by violating the reciprocal property or symmetry of the original Yee updating scheme.

4. NUMERICAL EXPERIMENTS

To begin with, late-time stability is examined in a rectangular resonator (RR). An air-filled region of $9 \times 8 \times 10$ mm, whose vertex points are located at the origin and $(9, 8, 10)$ mm, is surrounded by PEC plates. A SG region formed by two vertex points of $(2, 2, 2)$ and $(6, 5, 7)$ mm is embedded within the cavity in an asymmetric way. The MG cell size is $1 \times 1 \times 1$ mm, and the embedded SG region is initialized by a refinement factor of 3 in the NSG-H scheme. The circuit is simulated up to 1 million time steps. With CFL factor of 0.9,

late-time instability was observed within the simulation time period. By reducing the CFL factor to 0.7, we could remove the sign of late-time instability for both $T^C N^L$ and $T^Q N^L$ interpolation methods.

Next, basic reflection performance of the NSG-H scheme is investigated using an air-filled rectangular waveguide (RW) as in [8, 13]. With a refinement factor of 3, a sub-grid region of $20 \times 7 \times 20$ mm is embedded in a 20×7 mm RW. Reflection error is computed near the MG-SG interface. Fig. 7 depicts the reflection performance for three different discretization sizes. The sub-grid region constructed in a homogeneous region didn't show obvious reflection-performance difference with respect to interpolation methods in the NSG-H scheme. Considering difference in simulation setups such as the used refinement factor, we can say that the NSG-H scheme results in comparable reflection performance to the conservative method [8].

In the following sections, some practical microwave circuits are simulated in order to validate the improved performance and robustness of the NSG-H scheme in realistic and general problems. Along with stability and general applicability, computation efficiency and accuracy of the proposed subgridding scheme are mainly evaluated by comparison with results of two reference cases, i.e., entire coarse-mesh and fine-mesh simulations. The coarse and fine meshes have the same cell dimensions as those of MG and SG in the subgridding scheme, respectively. Identical refinement factor of 3 and CFL factor of 0.9 are used throughout all experiments. All microstrip circuits are surrounded by an air buffer region of 8 cells except 'zp' direction (12 cells) and the CPML region of 8 cells in all six directions. It

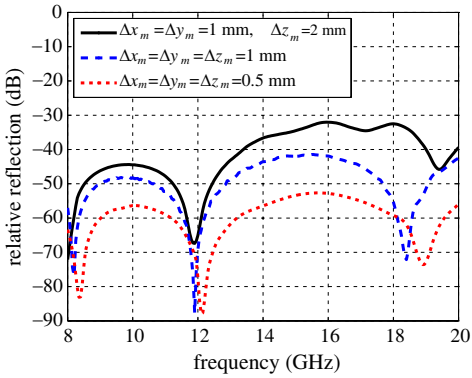

Figure 7. Computed relative reflection performance of the NSG-H scheme for three different discretization sizes in a 3-D rectangular waveguide example.

is noted that an air buffer region under the ground conductor of a circuit substrate, which is generally not necessary, is intentionally added in order to include the contribution of all six interfaces of a SG region. Results obtained by using frequency-domain commercial software *Sonnet Suites* [18] are also provided to confirm validity of the FDTD simulation.

For a direct comparison of accuracy performance with other existing subgridding schemes in [3–6], and [8–10], we tried to implement a few of existing schemes and simulated following examples in the same conditions, i.e., refinement factor of 3 and CFL factor of 0.9. However, most of the trials failed to obtain stable and meaningful results. For instance, schemes in [4–6, 10] showed weakness probably in handling a thin PEC plate traversing the interface, and schemes in [3, 9, 10] yielded instable results due to the lack of stability margin when the same CFL factor was used. Contrarily this implies robustness of the proposed subgridding scheme.

As a result, accuracy comparison is carried out in an indirect manner. The NSG-H scheme is compared with other two implemented schemes. One is the USG-E scheme which was shown in Fig. 3(a), and it can be regarded as the combination of methods in [6, 8]. The USG scheme basically uses E-field coupling of $T^C N^L$ method similar to [8], and the implicit complex coupling process in [8] is replaced by the explicit temporal and spatial coupling schemes used in [6]. The other one is the NSG-E scheme which was shown in Fig. 3(c) and discussed in the Section 3.1. This method modifies the coupling scheme of the USG-E suitable for the NSG mesh configuration. It is noted that both USG-E and NSG-E require the symmetric forward and backward coupling scheme to avoid late-time instability. By these combinations, material traverse capability and a sufficient stability margin can be obtained successfully and they can provide good reference data for accuracy comparison.

Relative accuracy can be estimated by calculating relative errors of each simulation result when it is compared with the result of uniform fine-mesh. For S-parameter results, the relative error metric [19] can be computed as

$$\varepsilon_S = \sqrt{\frac{\sum_k \sum_m \sum_n |S_{m,n}(f_k) - S^{ref}_{m,n}(f_k)|^2}{\sum_k \sum_m \sum_n |S^{ref}_{m,n}(f_k)|^2}}, \tag{14}$$

where f_k is a discrete frequency point, $S_{m,n}$ the S-parameters resulted by the simulation of a test case, and $S^{ref}_{m,n}$ the same S-parameters resulted by the simulation of the entire fine-mesh reference case.

4.1. Mitered Corner

To demonstrate applicability of the NSG-H scheme to a general subgridding case with a re-entrant corner, a transmission line having a mitered corner is simulated using three nonuniform SG regions, which are embedded within MG region by a refinement factor of 3. Fig. 8 shows the mitered transmission line and its spatial discretization in terms of coarse mesh or MG mesh. The circuit is constructed on the Alumina substrate with dielectric constant 9.9 and thickness of 1.016 mm. All simulations are performed for 1.32 ns (3000 MG or coarse-grid time steps, and 9000 SG or fine-grid time steps) with the voltage source excitation of a Gaussian waveform of $V_s = e^{\frac{-(t-t_0)^2}{\tau^2}}$, where τ is 8.47 ps and t_0 is set to 4.5τ. Algorithms implemented as a MATLAB code are executed on an Intel Core 2 Duo 2.2 GHz machine with a 4 GB physical memory. Fig. 9 shows the resulted S-parameters and relative error metrics which are calculated at each frequency point by $error_S(f_k) = |S_{m,n}(f_k) - S^{ref}_{m,n}(f_k)|$, and Table 1 summarizes the estimated computation times and relative errors. Fig. 9 and Table 1 are clearly showing that the NSG-H scheme can be applied to a complex and realistic case.

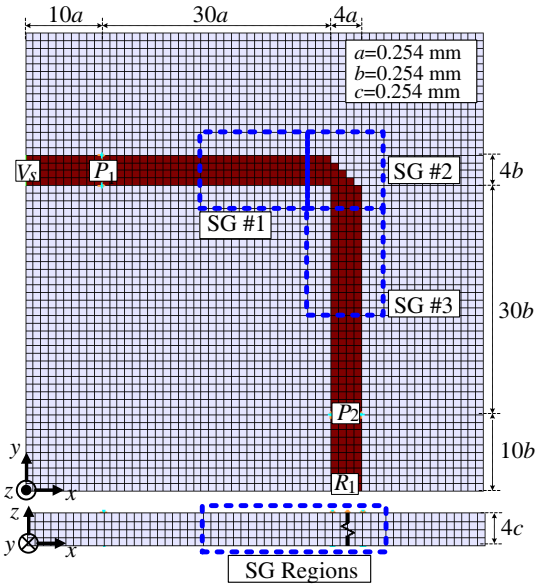

Figure 8. Geometrical illustration of the mitered transmission line example.

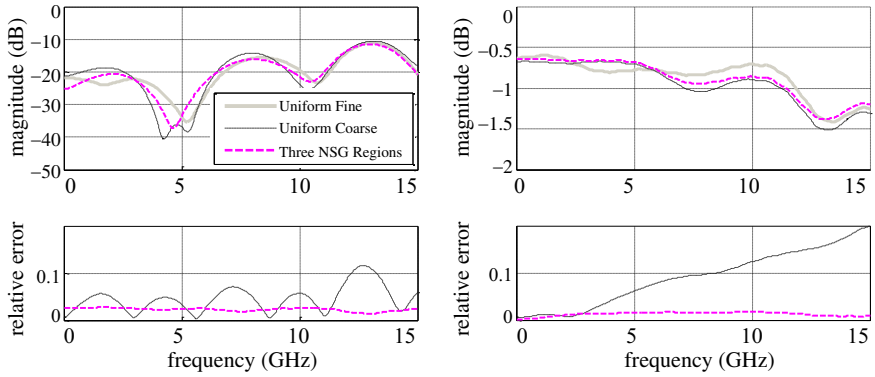

(a) S_{11} (b) S_{21}

Figure 9. Error estimation for the S-parameters of the mitered transmission line example.

Table 1. Comparison of error metric and CPU time in the mitered transmission line example.

	CPU Time (min)	ε_S		
		S_{11}	S_{21}	total
Uniform fine-mesh	386.2	-	-	-
Uniform coarse-mesh	13.4	0.3909	0.1183	0.1304
Three SG regions (NSG-H)	15.1	0.1700	0.0149	**0.0291**

4.2. Defected Microstrip Transmission Line

Defected microstrip structures (DMS) have narrowband band-stop responses similar to spur-line notch filters. Those structures are widely used as sub parts of distributed circuit blocks because of compactness and ease of integration. The circuit geometry is shown in Fig. 10(a), where only uniform coarse-mesh or MG is illustrated. The DMS is built on a substrate of dielectric constant 2.2, and the problem space is discretized to MG cells of $[\Delta x, \Delta y, \Delta z] = [0.406, 0.406, 0.265\,\text{mm}]$, and SG cells of a third of the MG cell size.

In all tests including fine-mesh, coarse-mesh, and subgridding cases, a voltage source is excited by a Gaussian waveform of $\tau = 13.54\,\text{ps}$, and simulations are performed for 1.75 ns, i.e., 3000 MG or 9000 SG time steps.

First of all, the reflection performance difference of $T^C N^L$ and $T^Q N^L$ methods with respect to MG-to-SG and SG-to-MG propagation

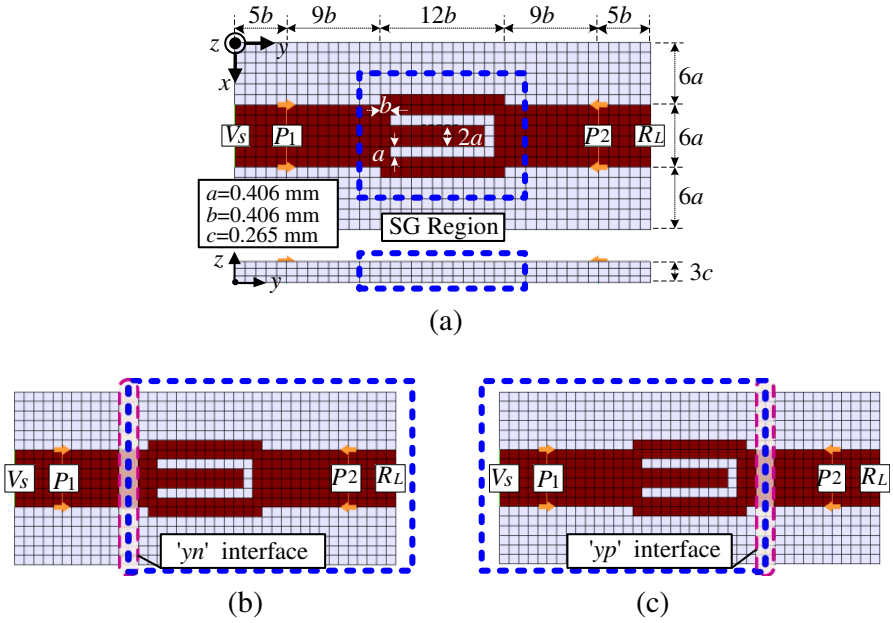

Figure 10. Geometrical illustration of defected microstrip transmission line, (a) the circuit dimensions, (b) MG-to-SG propagation at '*yn*' interface of SG region including load R_L, and (c) SG-to-MG propagation at '*yp*' interface of SG region including source V_s.

modes is verified through the tests shown in Figs. 10(b) and 10(c). The SG region in Fig. 10(b) includes the load, port 2, and the critical geometry region that needs finer mesh resolution, so that the '*yn*' interface is mostly working for the MG-to-SG mode. On the other hand, the second SG case in Fig. 10(c) embeds the voltage source, port 1, and the critical geometry region within the SG region. Thus, the excited wave is mostly propagating from the SG toward the MG region around the '*yp*' interface. $T^C N^L$ interpolation is applied to other interfaces except the specified '*yn*' or '*yp*' interface. For each case, resulted S_{11} is compared with the S_{11} reference obtained by entire fine-mesh simulation. As summarized in Table 2, $T^Q N^L$ and $T^C N^L$ methods show lower reflection errors in the MG-to-SG and SG-to-MG propagation cases, respectively.

Next, accuracy and efficiency of the NSG-H scheme are evaluated for the problem setup in Fig. 10(a). For comparison, aforementioned two subgridding schemes, i.e., USG-E and NSG-E, are also simulated.

Table 2. Comparison of reflection performance for MG-to-SG and SG-to-MG wave propagation modes in the DMS example.

MG-to-SG mode at 'yn' interface		**SG-to-MG** mode at 'yp' interface	
Interpolation method	$\varepsilon_S(S_{11})$	Interpolation method	$\varepsilon_S(S_{11})$
'yn' $T^C N^L$	0.1177	'yp' $T^C N^L$	0.0646
'yn' $T^Q N^L$	**0.0905**	'yp' $T^Q N^L$	0.0782

Table 3. Comparison of error metric and CPU Time in the DMS example.

	CPU Time (min)	ε_S		
		S_{11}	S_{21}	total
Uniform fine-mesh	192.7	-	-	-
Uniform coarse-mesh	10.5	0.4292	0.3416	0.3832
USG with E-coupling ($T^C N^L$)	14.4	0.1278	0.0482	0.0923
NSG with E-coupling ($T^C N^L$)	14.9	0.1367	0.0381	0.0955
NSG with H-coupling (Adaptive: yn/yp, elsewhere $T^C N^L$)	13.8	0.0801	0.0299	**0.0579**

In the simulation of the NSG-H, adaptive selection of $T^C N^L$ and $T^Q N^L$ is performed at 'yn' and 'yp' interfaces, whereas interpolation is fixed to $T^C N^L$ at the other interfaces. Fig. 11 depicts the resulted S-parameters and relative error metrics in the frequency range of 12 to 16 GHz. Computational efficiency and relative errors of three subgridding schemes are compared in Table 3. With a slight increase of computation time, all subgridding schemes yield more accurate results than the entire coarse-mesh. It is clear that the NSG-H scheme shows superior performance in accuracy. The accuracy improvement in the scheme is accomplished by both the optimal interpolation technique and the increased stability margin, which enables long-term stable simulations without employing symmetric backward coupling scheme.

4.3. Microstrip Low-pass Filter

The next example is a microstrip low-pass filter (LPF) whose geometrical dimension is indicated in Fig. 12. The same substrate of thickness 0.762 mm and dielectric constant 2.2 is used as in [1, 19, 20].

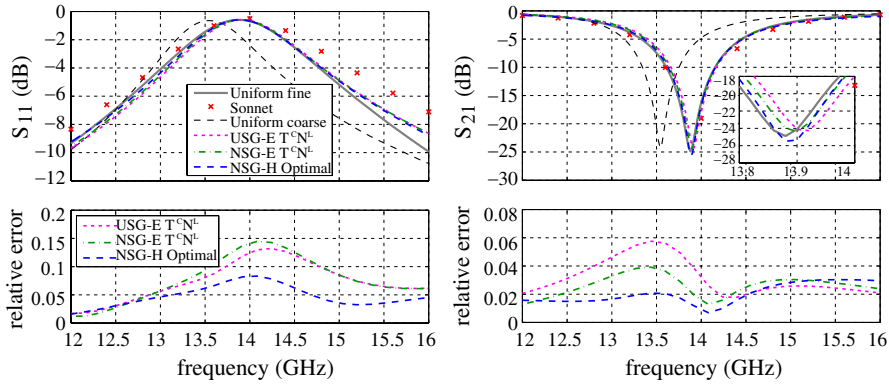

(a) S_{11} (b) S_{21}

Figure 11. Error estimation for the S-parameters of the DMS, obtained by three subgridding schemes.

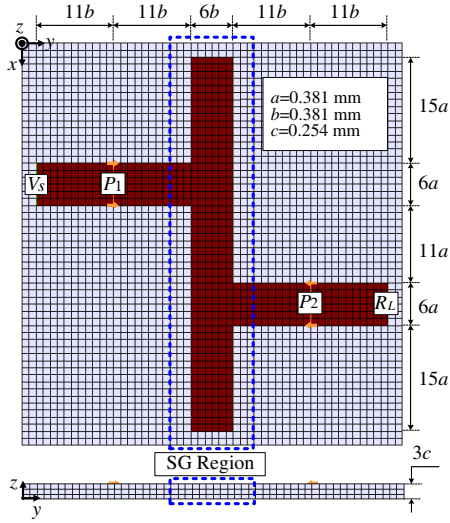

Figure 12. Geometrical illustration of microstrip low-pass filter example.

One sub-grid region is constructed in the central region of the problem space in order to include most of critical regions having circuit discontinuities such as T-junctions and open-ends. Similarly, a voltage source is excited by a Gaussian waveform of $\tau = 12.71$ ps. Simulations are performed for 1.66 ns, and a relative error metric is calculated using the resulted S-parameters up to 20 GHz.

Table 4. Comparison of error metric and CPU time in the LPF example.

	CPU Time (min)	ε_S		
		S_{11}	S_{21}	total
Uniform fine-mesh	530.8	-	-	-
Uniform coarse-mesh	24.9	0.1771	0.1138	0.1469
USG with E-coupling ($T^C N^L$)	43.6	0.1109	0.0254	0.0781
NSG with E-coupling ($T^C N^L$)	41.0	0.1140	0.0280	0.0807
NSG with H-coupling (Adaptive: yn/yp, elsewhere $T^C N^L$)	39.2	0.0729	0.0284	**0.0540**

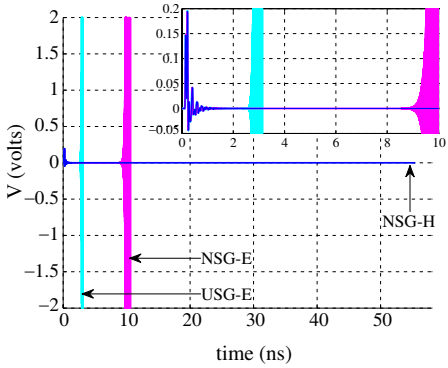

Figure 13. Sampled voltages at port 2 in three subgridding schemes employing a simple backward coupling. Nonuniform subgridding scheme with H-coupling shows superior stability factor.

In this LPF example, numerical experiments are executed for sufficiently long time steps to test the generic stability margin of each subgridding scheme. When the USG-E and the NSG-E employ the symmetric coupling scheme, each scheme doesn't show any instability sign up to 200000 time steps. On the other hand, the USG-E and the NSG-E show oscillation when the symmetric backward coupling scheme is intentionally disabled for fair comparison and appropriate simple averaging schemes are applied. At this case, the USG-E and the NSG-E yield oscillations at 4500 and 15000 time steps. Fig. 13 depicts voltages sampled at the port 2, and verifies that the stability factor is effectively enhanced by the NSG mesh, especially with H-coupling.

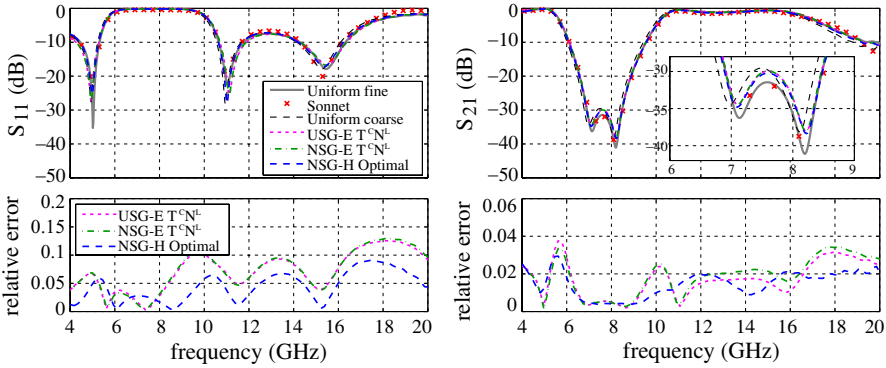

(a) S_{11} (b) S_{21}

Figure 14. Error estimation for the S-parameters of the LPF, obtained by three subgridding schemes.

For a similar estimation of computational efficiency and relative accuracy, performance comparison is shown in Table 4 and Fig. 14. From Table 4, we can see that the NSG-H scheme yields the most accurate S-parameter results, whereas the other two schemes show similar accuracy. In addition, CPU time in the proposed scheme is less than or equal to that in the others even though additional computation is included for an adaptive selection algorithm.

5. CONCLUSION

We have proposed a nonuniform sub-grid (NSG) mesh configuration to increase the stability margin by separating interpolation-error and dislocation-error planes. The nonuniform subgridding scheme with H-coupling (NSG-H) improves simulation accuracy by employing a simple backward coupling scheme without late-time instability. Its accuracy is further optimized by applying an adaptive interpolation technique. The subgridding scheme also enables efficient simulation using higher factor of the CFL time step limit. Robustness against material discontinuities at transition interfaces, as well as stability, accuracy, and efficiency, has been verified by three realistic microstrip applications.

REFERENCES

1. Elsherbeni, A. and V. Demir, *The Finite-difference Time-domain Method for Electromagnetics with MATLAB Simulations*, SciTech Publishing, Inc., Raleigh, NC, 2009.
2. Courant, R., K. Friedrichs, and H. Lewy, "On the partial difference equations of mathematical physics," *IBM Journal of Research and Development*, Vol. 11, No. 2, 215–234, 1967.
3. Thoma, P. and T. Weiland, "A consistent subgridding scheme for the finite difference time domain method," *Int. J. Numer. Modeling: Electron. Networks, Devices Fields*, Vol. 9, 359–374, 1996.
4. Krishnaiah, K. and C. Railton, "A stable subgridding algorithm and its application to eigenvalue problems," *IEEE Trans. Microw. Theory Tech.*, Vol. 47, No. 5, 620–628, May 1999.
5. Xiao, K., D. Pommerenke, and J. Drewniak, "A three dimensional FDTD subgridding algorithm based on interpolation of current density," *Proc. IEEE EMC Symp.*, Vol. 1, 118–123, Santa Clara, CA, 2004.
6. Xiao, K., D. Pommerenke, and J. Drewniak, "A three-dimensional FDTD subgridding algorithm with separated temporal and spatial interfaces and related stability analysis," *IEEE Trans. Antennas Propagat.*, Vol. 55, No. 7, 1981–1990, Jul. 2007.
7. Monk, P., "Subgridding FDTD schemes," *Appl. Comput. Electromagn. Society J.*, Vol. 11, No. 1, 37–46, 1996.
8. Chilton, R. A. and R. Lee, "Conservative and provably stable FDTD subgridding," *IEEE Trans. Antennas Propagat.*, Vol. 55, No. 9, 2537–2549, Sep. 2007.
9. Chevalier, M. W., R. J. Luebbers, and V. P. Cable, "FDTD local grid with material traverse," *IEEE Trans. Antennas Propagat.*, Vol. 45, 411–421, Mar. 1997.
10. White, M. J., Z. Yun, and M. F. Iskander, "A new 3-D FDTD multigrid technique with dielectric traverse capabilities," *IEEE Trans. Microw. Theory Tech.*, Vol. 49, 422–430, 2001.
11. Vaccari, A., R. Pontalti, C. Malacarne, and L. Cristoforetti, "A robust and efficient subgridding algorithm for finite-difference time-domain simulations of Maxwell's equations," *J. Comp. Phys.*, Vol. 194, 117–139, 2004.
12. Donderici, B. and F. L. Teixeira, "Improved FDTD subgridding algorithms via digital filtering and domain overriding," *IEEE Trans. Antennas Propagat.*, Vol. 53, No. 9, 2938–2951, 2005.

13. Kulas, L. and M. Mrozowski, "Low reflection subgridding," *IEEE Trans. Microw. Theory Tech.*, Vol. 53, No. 5, 1587–1592, 2005.
14. Berenger, J.-P., "A Huygens subgridding for the FDTD method," *IEEE Trans. Antennas Propagat.*, Vol. 54, 3797–3804, 2006.
15. Moler, C., *Numerical Computing with MATLAB*, 2004, Available: http://www.mathworks.com/moler/index_ncm.html.
16. Okoniewski, M., E. Okoniewska, and M. A. Stuchly, "Three-dimensional subgridding algorithm for FDTD," *IEEE Trans. Antennas Propagat.*, Vol. 45, No. 3, 422–429, 1997.
17. Kermani, M. H. and O. M. Ramahi, "The complementary derivatives method: A second-order accurate interpolation scheme for nonuniform grid in FDTD simulation," *IEEE Microw. Wireless Compon. Lett.*, Vol. 16, 60–62, Feb. 2006.
18. *Sonnet User's Guide — Release 12*, Sonnet Software Inc., North Syracuse, NY, Apr. 2009.
19. Liu, Y. and C. D. Sarris, "Efficient modeling of microwave integrated circuit geometries via a dynamically adaptive mesh refinement (AMR) — FDTD technique," *IEEE Trans. Microw. Theory Tech.*, Vol. 54, No. 2, 689–703, Feb. 2006.
20. Sheen, D. M., S. M. Ali, M. D. Abouzahra, and J. A. Kong, "Application of the three-dimensional finite-difference time-domain method to the analysis of planar microstrip circuits," *IEEE Trans. Microw. Theory Tech.*, Vol. 38, 849–857, Jul. 1990.